Journal of Materials Chemistry A

ROYAL SOCIETY OF CHEMISTRY

PAPER

View Article Online
View Journal | View Issue

Cite this: J. Mater. Chem. A, 2026, 14, 12173

FeO-enabled low-temperature CO_2-splitting for chemical looping carbon utilization

Huang-Chin Lin,† Yi Chen,† Tzu-Hao Hung, Ding-Huei Tsai, Lu-Yu Chueh, Chun-I Chou, Kun-Han Lin * and Yung-Tin (Frank) Pan *

Received 27th September 2025
Accepted 5th February 2026

DOI: 10.1039/d5ta07934a

rsc.li/materials-a

Chemical looping integrated with CO_2 utilization is an attractive chemical process that can contribute greatly to on-site carbon capture and utilization. To reduce the excess energy consumption, the kinetics of the CO_2-splitting half reaction has been revisited on pure iron oxygen carriers. High CO_2-splitting rate at a very low temperature of 350 °C is discovered with an unambiguous relationship to the presence of FeO. Through controlled reduction, a nanoporous oxygen carrier enriched with active FeO, capable of 2-dimensional oxide growth with fast kinetics is formed and can be regenerated under cycling conditions of a chemical looping reverse water–gas shift model reaction at 500 °C. Over-reduction leads to the formation of low activity metallic Fe that requires additional 100 °C or more to conduct CO_2-splitting, which deactivates rapidly due to severe sintering. Density functional theory calculations reveal the minimum energy pathway involving the dissociation of adsorbed CO_2 on the Fe surface, followed by the spillover of CO to the FeO surface for desorption. These findings provide guidance for the design of a reactive iron-based oxygen carrier for low temperature CO_2-splitting in all chemical looping carbon capture utilization processes.

Introduction

Decarbonization of the power, transportation, and industrial sectors is vital for the success of a net-zero emission scenario before 2050 to withhold the rise of global temperature within the 2 °C limit. On-site carbon capture and utilization (CCU) would be a preferable way to mitigate carbon emissions from centralized large-scale sources such as fossil fuel power plants. This is because the energy penalty for CCU can potentially be compensated with proper heat integration.[1,2] The optimum case would be the use of low-grade waste heat to drive such CCU processes.

Hydrogenation of CO_2 to value-added chemicals is a plausible approach for CCU in the presence of affordable hydrogen (H_2). CO_2 can be hydrogenated to form methane *via* the nickel-catalyzed methanation reaction at relatively low pressure and temperature.[3–6] It can also be converted to CO *via* the reverse water–gas shift (RWGS) reaction at low pressure and higher temperatures in the presence of copper or iron catalysts.[7,8] With additional expense for compression, CO_2 can also be hydrogenated into methanol using copper-based catalysts at much higher pressures.[9,10] For these catalytic conversions of CO_2 to be economically feasible, high yield and product selectivity is required to minimize down-stream separation cost. In this aspect, the chemical looping method provides a better opportunity to regulate product selectivity with very high precision.[11–17] Since the redox chemistry is now mediated by the oxygen carrier, co-existence of CO_2 and H_2 in the reactor is not required. The reaction proceeds in two-steps where the reduced-form oxygen carrier splits CO_2 into CO and the oxidized-form oxygen carrier oxidizes H_2 into H_2O, both specifically.[18–22] Since the two-steps are temporally and spatially separated, down-stream separation can be omitted. Furthermore, the CO_2-splitting half-reaction, in principle, can be coupled with any desirable oxidation half reactions such as the partial oxidation of alkanes.[23]

The key component of a successful chemical looping process is an active oxygen carrier with good structural reversibility. For the CO_2 splitting half reaction, various transition metal oxides,[13,19,24–26] spinel oxides,[27,28] perovskite oxides,[23,29,30] and others[31,32] have been investigated. Within the wide variety of elements and crystal structures, iron serves as the critical element that conducts redox chemistry with CO_2. For example, earlier studies by Galvita revealed the reversible phase change of iron-based oxygen carriers between Fe_3O_4/FeO/Fe during H_2 temperature programmed reduction (H_2-TPR) and CO_2 temperature programmed oxidation (CO_2-TPO) by *in situ* XRD.[13,21] Based on the TPR/TPO results, constant temperature looping was conducted at 600 °C. A recent study by Xiao demonstrated high CO_2-splitting activity using Cu/Mn/Co-doped spinel ferrites at 650 °C.[24,28] Li reported the use of Cu-doped $LaFeO_3$ perovskite to conduct CO_2 splitting in the

Department of Chemical Engineering, National Tsing Hua University, 101 Sec. 2, Kuang-Fu Rd, Hsinchu City, 300044, Taiwan. E-mail: ytpan@mx.nthu.edu.tw; kunhan.lin@mx.nthu.edu.tw

† These authors contributed equally to this work.

presence of O_2 at 850 °C.[33] Zhao reported the use of Ce-modified $SrFeO_{3-\delta}$ to conducted CO_2 splitting coupled with ethane oxidative dehydrogenation at 725 °C.[29] Obviously, it would be more desirable to conduct the looping process at lower temperatures, but attempts at temperatures below 600 °C remain scarce.

To achieve this goal, we have revisited the redox chemistry and phase behavior of pure iron oxides, seeking opportunities to decipher the key descriptor that enables low-temperature chemical looping CCU. We proved that fast kinetics of CO_2 splitting at low temperature is possible and revealed its unambiguous strong correlation with the presence of the *meta*-stable wüstite FeO. Using the chemical looping reverse water–gas shift (CL-RWGS) as a model reaction, we have identified the optimum matching of CO_2 splitting and H_2-oxidation half reaction conditions. By applying the general kinetic model for grain boundary nucleation and growth, distinctive 2-D growth and fast oxidation kinetics were discovered for the oxygen carriers treated with short H_2 durations. CO_2-TPO revealed a highly reactive species, having a peak temperature below 350 °C, which is accountable for the fast CO_2-splitting kinetics. Detailed crystallography analysis pointed out the likelihood of FeO being accountable for the high reactivity, for which its generation and regeneration was more effective with shorter H_2 steps. With extended H_2 step duration, FeO was no longer preserved, and the fast CO_2-splitting kinetic feature of the reduced oxygen carrier was lost.

Experimental

Materials and chemicals

Iron(III) nitrate nonahydrate ($Fe(NO_3)_3 \cdot 9H_2O$, 98%, Alfa-Aesar); ammonium hydroxide ($NH_4OH_{(aq)}$, 30–33%, Honeywell); deionized water (DI water, from Merck Millipore Milli-Q, 18.2 MW resistance); hydrogen gas (H_2, 5%, 4N-grade, Sinda Gas Corp.); carbon dioxide (CO_2, 10% balanced with argon, 4N-grade, Sinda Gas Corp); argon (Ar, 4N-grade, Sinda Gas Corp.)

Preparation of iron oxide oxygen carriers

The pristine iron oxide oxygen carriers in the present study were prepared by a direct precipitation method, as reported in previous studies.[18] In a typical process, 0.015 mol of $Fe(NO_3)_3 \cdot 9H_2O$ was first dissolved in 50 mL of DI water. Under vigorous stirring conditions, the solution was titrated with 1 M ammonium hydroxide to pH 9 and maintained at this pH for another 30 min. The precipitated products were then separated by centrifugation and washed with DI water through repetitive dispersion/centrifugation cycles until the pH of the supernatant approached 7. The samples were then dried in an 80 °C vacuum oven overnight. The dried samples were ground using a mortar and pestle to fine powders and subjected to a 3 h thermal treatment in air at 500 °C to yield the final powder samples.

Characterization

Powder X-ray diffraction (PXRD, D8A25, Bruker) was conducted to characterize the crystal phase of the oxygen carriers during different stages of their lifetime. Refinement of XRD patterns was conducted using GSAS. Field emission scanning electron microscopy (FESEM, SU8010, Hitachi) was carried out to image the morphological features of the oxygen carriers at 20 kV. Scanning transmission electron microscopy (STEM, JEM-F200, JEOL) was conducted at an accelerating voltage of 200 kV from the cold field emission gun to image the nanoscale features of the oxygen carriers. A coupled energy dispersive X-ray spectrometer was used to conduct spatial and quantitative elemental analysis.

Chemical looping testing, temperature programmed oxidation in CO_2, and product analysis

The chemical looping reverse water–gas shift reaction and CO_2-TPO were both conducted using a home-built reaction and analysis system. The reaction system includes three mass flow controllers (SLA5850E, Brooks), a 4-inch diameter U-shape quartz tube, and a tube furnace (custom-built, GL-Glass). A packed bed reactor was configured by placing 100 mg of powder oxygen carrier samples inside the U-shape quartz tube and immobilized between two pieces of quartz wool. During a typical chemical looping process, once the packed bed reactor is placed inside the tube furnace, Ar was then purged into the reactor at 300 sccm for 10 min to remove residual air. The reactor was then ramped up to certain temperature with a ramp rate of 10 °C min^{-1}. The chemical looping process was then conducted isothermally by introducing 5%-H_2 and 10%-CO_2 alternatively with a 3-min Ar purge step in between, all at a flow rate of 300 sccm. The gaseous products exiting the reactor were analyzed using a CO_2 non-dispersive infrared spectrometer (NDIR, CI-IR 20, Chang-AI), a CO-NDIR (CI-IR 20, Chang-Ai), and a thermal conductivity detector (TCD, CU-TC 90, Chang-AI) to quantify CO_2, CO, and H_2 with ms resolution. The CO_2-TPO was conducted with a process similar to the chemical looping reverse water–gas shift reaction except that the CO_2 steps in certain cycles were carried out with a temperature ramp from 150 °C to 500 °C instead of isothermally at 500 °C.

Computational details

All periodic DFT computations were carried out using the Vienna *Ab initio* Simulation Package (VASP),[34–37] while electronic structure analyses were conducted with the post-processing VASPKIT package.[38] The Perdew–Burke–Ernzerhof (PBE) functional within the framework of generalized gradient approximation (GGA)[39,40] was employed to model the exchange–correlation interactions in pure Fe systems. For the remaining systems, additional corrections—including Hubbard *U*, spin–orbit coupling (SOC), and D3(BJ) dispersion—were incorporated, as described in detail in the Results and discussion section and SI. Projector augmented wave (PAW) potentials were used to account for electron–ion interactions.[41,42] A plane-wave energy cutoff of 520 eV was consistently applied across all calculations. To treat Fermi surface broadening, the Methfessel–Paxton smearing scheme[43] was adopted, with a smearing width of 0.20 eV for pure Fe systems, while a Gaussian smearing width of 0.04 eV was applied for Fe surfaces with adsorbates and

for FeO systems. Geometric relaxations were performed using the conjugate gradient method, and convergence was reached when all atomic forces dropped below 0.02 eV $Å^{-1}$. Monkhorst–Pack *k*-point mesh was adjusted based on the specific slab dimensions, as detailed in the Results and discussion section and SI. A vacuum region of 15 Å was introduced perpendicular to the slab surface in all models to eliminate spurious interactions between periodic images. All reported energy values were extrapolated to 0 K. Spin polarization was explicitly considered for Fe atoms throughout the surface calculations. In addition, Bader charge analysis was performed only for FeO systems, as detailed in the Results and discussion section and SI.[44–48] Most of the structural visualizations were generated using Crystal Toolkit developed by A. Jain *et al.*[49]

Results and discussion

Regenerative CO_2-splitting of iron oxygen carriers through optimized looping programs

The performance of CL-RWGS using Fe-oxygen carriers is strongly associated with the reversibility of its redox chemistry, which is heavily dependent on the reaction conditions and history. Preliminary studies on the CO_2-splitting activity and cycle stability suggested that under a fixed H_2/CO_2 program of 5 min/10 min, a process temperature of 500 °C is optimal for obtaining the highest instantaneous CO concentration during the CO_2-splitting step due to the balanced reduction and oxidation kinetics of the oxidized and reduced Fe-oxygen carriers respectively (Fig. S1). The rather low 500 °C operation is beneficial from the viewpoint of utilizing industrial waste heat to conduct the chemical looping CO_2 utilization process. However, to optimize performance and cycle stability, the H_2/CO_2 program was further studied systematically by varying duration of the H_2 step while fixing the CO_2 step at 10 min. Using homemade Fe_2O_3 as the starting material, the program with a 1-min H_2 step showed good cycle stability but the amount of CO produced in the CO_2-splitting step was too little due to the limited amount of reduced-form Fe species formed during the short exposure to H_2. When increasing the H_2-step duration to 3 min, the CO_2-splitting reaction was completed within two minutes as the CO concentration measured by the non-dispersive infrared (NDIR) detector approached the baseline level (Fig. 1a, S2 and S3). The maximum instantaneous CO concentration can reach up to 1.3%, equivalent to 13% of CO_2 conversion and gradually decreased to 0.9% after fifteen cycles. When the H_2-step duration was increased to 5 min, a similar behavior of the CO production can be observed but the maximum CO concentration was increased to 1.4% and approached the baseline level after 5 min with a transition stage in between (Fig. 1b). The most apparent difference lies in the width of the CO peak, which increased from 43 s to 68 s and ended up having higher CO_2-splitting capacity in each cycle. The CO_2-splitting behavior was significantly altered when the H_2 step was increased to 7 min. Although the maximum CO concentration can reach up to 1.5% in early stages, a rapid loss of the CO peak concentration in successive cycles occurred and was accompanied by the appearance of slow-kinetic CO production in the range of 0.2–0.3% throughout the later stages (Fig. 1c). A similar behavior was observed when the H_2 step duration was extended to 10 min. However, the CO peak width was further increased to 90 s and the slow kinetic CO production started to take place even in the first cycle (Fig. 1d). When the H_2 step was further extended to 60 min, the CO_2-splitting behavior became drastically different. Except for the first cycle, both the maximum CO concentration and the slow kinetic CO production were significantly smaller than previous cases

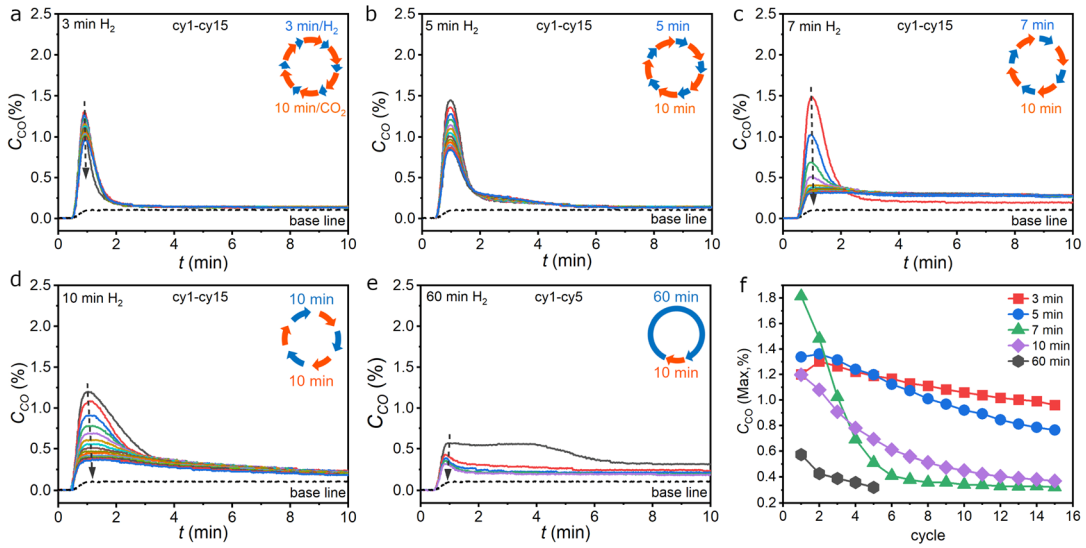

Fig. 1 Recorded real-time CO concentration during the CO_2-splitting step with different redox programs using Fe-oxygen carriers to conduct CL-RWGS at 500 °C. (a) $H_2/CO_2 = 3$ min/10 min, (b) $H_2/CO_2 = 5$ min/10 min, (c) $H_2/CO_2 = 7$ min/10 min, (d) $H_2/CO_2 = 10$ min/10 min, and (e) $H_2/CO_2 = 60$ min/10 min. (f) A summary of the CO peak concentrations recorded in (a–e). Conditions: 300 sccm CO_2 (10% balanced with Ar), 300 sccm Ar (4N-grade), and 300 sccm H_2 (5%, balanced with Ar).

(Fig. 1e). The dynamic variations of CO production using different programs are summarized in Fig. 1f by plotting the maximum CO concentration against the number of cycles. The CO peak concentration was much better maintained over successive cycles with programs of short H_2 steps and can be maintained over 0.48% after 50 cycles for the 5 min/10 min program (Fig. S4). As the H_2 step duration exceeded 5 min, rapid loss of the CO peak concentration, *i.e.*, CO_2-splitting kinetics, occurred.

Oxidation kinetics of iron oxygen carriers in CO_2

Since the rate of CO_2-splitting should be equivalent to the rate of Fe (or FeO) oxidation, kinetic models developed for reactions of Fe with gaseous species can be implemented here to aid the understanding of experimental observations. According to Hancock and Sharp's method,[50,51] isothermal solid-state reactions can be compared based on the general equation for nucleation and growth on phase boundaries:

$$\alpha = 1 - e^{-kt^n} \quad (1)$$

$$\ln(-\ln(1-\alpha)) = \ln k + n \ln t \quad (2)$$

where α is the conversion of Fe at a certain time t, k is a constant that depend on both the nucleation frequency and the grain growth rate, and n is the exponent associated with the growth dimension.[52,53] Under the assumption that the conversion of CO_2 is equivalent to the conversion of Fe, the real time CO concentration monitored by NDIR can be used to derive α during each CO_2-splitting step. Using the total amount of CO produced in the 1st cycle, the α–t relation in each cycle for each program is constructed (Fig. 2a–e). Obvious differences in the α–t curves can be observed for short H_2-programs, *i.e.*, programs with 3 min and 5 min H_2 steps, which show sharp transitions between the kinetic-controlled acceleration and the diffusion-controlled deceleration stages. The active species in these two stages are referred to as the "fast-kinetic" and "slow-kinetic" species hereafter. Loss in overall conversion can be attributed to the loss of fast-kinetic species in the reduced oxygen carrier. When increasing the H_2 step to 7 min, a similar transition was observed in the first two cycles. However, the fast kinetic features became absent with linear α–t relations after the 6th cycle. Interestingly, most of the fast-kinetic species were transformed into slow kinetic species instead of becoming completely inactive. In the case of a 10-min H_2 step, oxidation was still composed of two different events with lower rates for both the kinetic and diffusion-controlled steps. However, severe deactivation of both the fast and slow-kinetic species had resulted in nearly 50% of initial conversion lost after 15 cycles. Finally, in the 60-min H_2-program, the 1st cycle showed a transition around 4.5 min while the 3rd and 5th showed a very early transition at $\alpha < 5\%$, accompanied by more than 60% loss of the initial conversion. Based on eqn (2), plots of $\ln(-\ln(1-\alpha))$ against $\ln(t)$ were constructed for each curve in Fig. 2a–e in the range of $\alpha = 0.15$–0.3 to obtain more insights into the kinetic-controlled, *i.e.*, the high-rate region of Fe oxidation (Fig. S5). In this analysis, the conversion of each cycle was normalized individually to compare the intrinsic kinetics of the remaining reactive species. In such a plot, the slope of the curve is the n-value, which is generally interpreted as the sum of $l + d$, where l is the dimensionality of growth (*i.e.*, 1, 2, or 3) and d is the contribution of the nucleation process to the overall kinetics. d varies between 0 and 1, where 0 corresponds to instantaneous nucleation and 1 to very slow nucleation. The intercept is $\ln(k)$, which can be used to determine the kinetic rate constant. The obtained n and k-values are summarized in Fig. 2f and g, respectively. Both the n and k-values of the 3 min/10 min program are distinctively larger compared with others. The obtained n values range from 2.41 to 2.17, which suggested a 2-D growth of the Fe-oxide during the CO_2-splitting step.[53] When

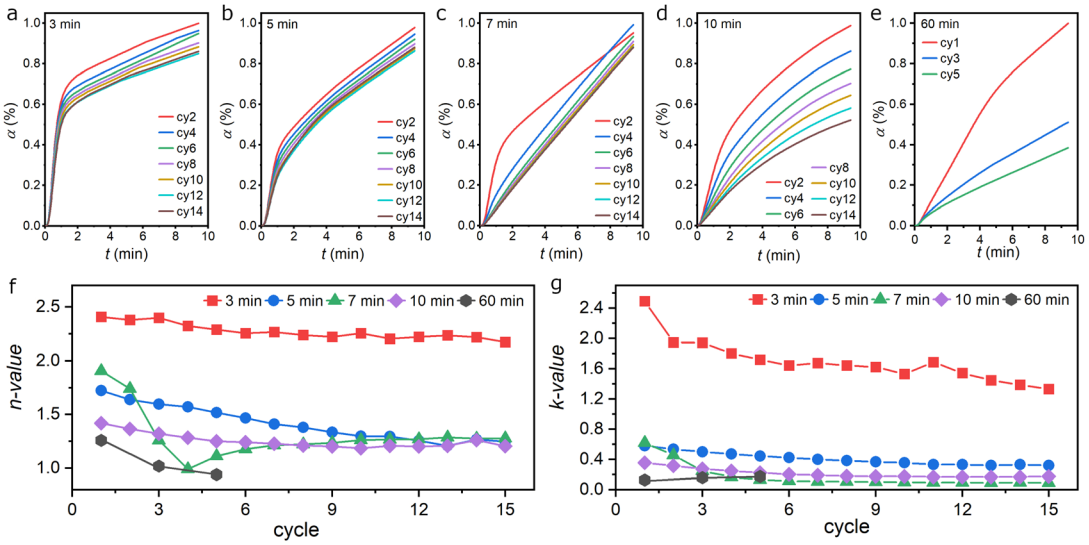

Fig. 2 Oxidation kinetics of reduced-form Fe-oxygen carriers subjected to programs with varying H_2 step durations. (a–e) Plots of conversion (α) against t. (f and g) Plots of the n-value and k-value of over successive cycles for the 3 min/10 min, 5 min/10 min, 7 min/10 min, 10 min/10 min, and 60 min/10 min programs, respectively.

H_2-step duration was prolonged to 5 min and beyond, the obtained n values were all below 2, suggesting that commonly reported 1-D oxide growth was occurring. In general, the n-values for all programs were decreasing with successive cycles. This suggested that the formation of new nuclei was contributing less and less after repetitive cycling except for the 7 min/10 min program, showing a rapid decrease in the first four cycles and a gradual increase back to a level around 1.27. Furthermore, in the 5th cycle of the 60 min/10 min program, the n-value became 0.97, *i.e.* <1, meaning diffusion had become the governing factor of Fe oxidation.[52] On top of the additional growth dimension, the rate constants (k-value) of the 3 min/10 min program were also significantly larger than others. It started from 2.49 min^{-1} in the 1st cycle and gradually decreased to 1.33 min^{-1} in the 15th cycle. These values are approximately 4 times larger than those obtained from the 5-min H_2 program and 7–19 times larger than the programs with even longer H_2-steps. From the above kinetic analysis, the fast-kinetic 2-D growth synergy created from the short 3 min H_2 steps resulted in the observed high CO_2-splitting reactivity. This was confirmed in a separate experiment in the first 5 cycles even though the capacity loss was greater in this separately prepared Fe oxygen carrier sample (Fig. S6).

Thermo-chemical properties and their relation to the crystal phase studied *via* CO_2-temperature programmed oxidation and powder X-ray diffraction

The observed variations in CO_2-splitting kinetics with different redox programs are likely due to the dynamic phase composition of the Fe oxygen carriers in different reaction environments. To gain further understanding, CO_2-TPO and post-mortem PXRD were conducted on the Fe oxygen carriers after certain cycles of the CL-RWGS process (please refer to Fig. S7, S8 and SI Note 1 for the raw data and smoothing protocol). In general, the CO_2-TPO curves are composed of a low temperature α peak around 350 °C and a high temperature β peak around 475 °C, showing a high correspondence to the "fast-kinetic" and "slow-kinetic" species identified previously. The relative ratio between the α and β peaks decreased in the programs with

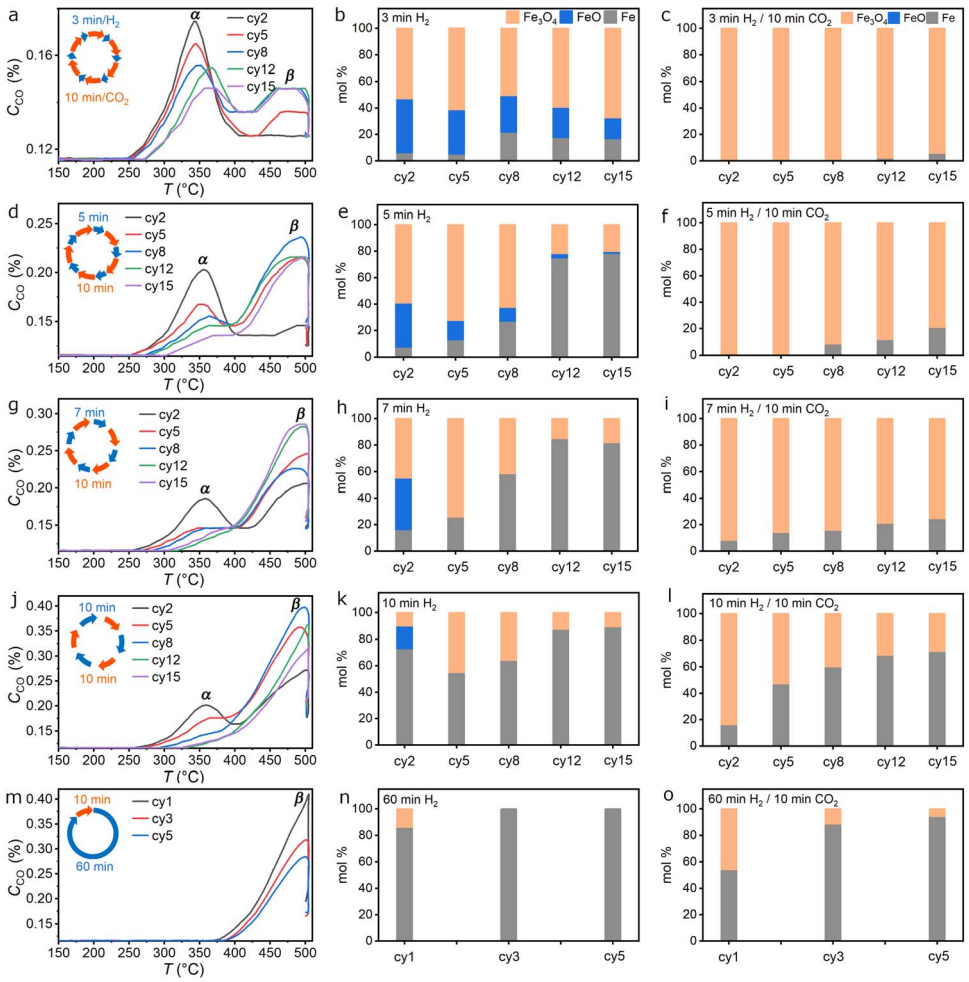

Fig. 3 Thermal oxidation and crystallographic study of the Fe-based oxygen carriers subjected to programs with varying H_2 step durations. (a) CO_2-TPO profiles after selected cycles and corresponding mole fractions of Fe, FeO, and Fe_3O_4 of the Fe oxygen carrier after the (b) reduction and (c) oxidation steps, respectively, using a H_2/CO_2 program of 3 min/10 min. Same type of data as presented in (a–c) except with H_2/CO_2 programs of (d–f) 5 min/10 min, (g–i) 7 min/10 min, (j–l) 10 min/10 min, and (m–o) 60 min/10 min.

longer H_2-steps. This α/β ratio also decreased in successive cycles in individual programs. Corresponding PXRD patterns confirm that CL-RWGS was associated with the redox processes between metallic Fe, wustite FeO, and spinel Fe_3O_4 (Fig. S9). For the 3 min/10 min program, the β peak was absent at initial stages and appeared after the 5th cycle, accompanied by the increased peak temperature and decreased intensity of the α peak (Fig. 3a). From PXRD refinement results, the reduced-form oxygen carrier in the 3 min/10 min program was originally dominated by FeO, reaching 40.8% after the 2nd cycle and gradually decreased to 15.7% after the 15th cycle (Fig. 3b). The Fe content increased complementary from 6.1% after the 2nd cycle to 21.6% after the 8th cycle and decreased to 16.8% after the 15th cycle. Although decreasing in its fraction, the regenerative formation of FeO was observed even though being reported thermodynamically unstable at 500 °C.[54,55] After the CO_2 steps, the Fe oxygen carrier was composed of Fe_3O_4 except with a small fraction of unreacted Fe after the 15th cycle (Fig. 3c). To figure out the oxidation process associated with the α-peak, the CO_2-TPO was cut-off before the β-peak appeared. PXRD patterns of the corresponding oxygen carrier at different cycles showed only peaks for Fe_3O_4 and Fe, confirming that oxidation of FeO is an important contributor to the fast CO_2-to-CO kinetics (Fig. S10, Eq. (3)).

$$3FeO + CO_2 \rightarrow Fe_3O_4 + CO \quad (3)$$

The statement is strengthened from the systematic study of the oxygen carrier experiencing longer H_2 steps, where the ratio of α/β peaks in the CO_2-TPO correlated positively with the FeO/Fe ratio consistently. For the 5 min/10 min program, the α peak and FeO content in the reduced oxygen carrier gradually decreased to zero as Fe became the dominant phase after the 8th cycle (Fig. 3d and e). However, not all Fe was converted back to Fe_3O_4, explaining the loss in CO_2-splitting capability due to the formation of inactive Fe species over time. In the 7 min/10 min program, Fe had become the dominant phase with no FeO just after the 5th H_2-step (Fig. 3g and h). It was unique in that most of the formed Fe here, although showing slow kinetics, remained reactive throughout the 15 cycles (Fig. 3i). The formation of inactive Fe became severe when the H_2-step duration passed the 10-min threshold (Fig. 3j–l). Further extension of the H_2-step to 60 min eliminated the formation of FeO and led to the formation of nearly inactive Fe after the 3rd cycle (Fig. 3m–o). In addition to the fractional distribution of Fe and FeO, the grain size of each of the phases can also be obtained from the PXRD patterns. The mole fraction and grain size of Fe and FeO, *i.e.*, reduced-form oxygen carriers, are summarized with respect to the number of cycles (Fig. S11, S12 and Table S1, SI Note 2).

Theoretical investigation of CO_2-splitting

To rationalize the observed irreversibility and the coexistence of fast and slow kinetics in our experiments, we first aimed to establish a reliable theoretical description of the electronic structure of FeO as a prerequisite for surface adsorption modeling. Because FeO is a prototypical Mott insulator, conventional generalized-gradient approximation (GGA) functionals significantly underestimate its band gap and fail to reproduce its insulating nature.

We therefore benchmarked the PBE + U approach, with and without spin–orbit coupling (SOC), by systematically varying the Hubbard U parameter and comparing the resulting lattice parameters and band gap against experimental values. Based on this benchmark, we selected a PBE + U ($U = 3.7$ eV) with SOC setup for the remainder of the calculations. Full computational details and the benchmarking results are provided in SI Note 3 and Note 4 (Tables S2–S4 and Fig. S13, S14). We first examined plausible adsorption configurations of CO_2, CO, and O (denoted as CO_2^*, CO^*, and O^*) on the Fe(100) and FeO(100) surfaces. Fig. 4 summarizes the most stable adsorption geometries identified for each adsorbate across the investigated surfaces. Full details—including all configurations screened, the definition and evaluation of adsorption energies (E_{ads}), and the dissociative chemisorption energy (ΔE_{chem})—are provided in SI Note 5. Monkhorst–Pack k-point mesh was adjusted based on the specific slab dimensions, as detailed in Tables S4 and S5. This accurate reproduction of the electronic band structure serves as a proof of method, ensuring the reliability of subsequent adsorption calculations. Fig. 4 and 5 presents the reaction energy diagram for CO_2 splitting on Fe(100) and FeO(100) surfaces. CO_2 chemisorbs exothermically on both surfaces, with slightly stronger binding on Fe(100) (~0.48 eV more negative) than on FeO(100).

Upon adsorption, the chemisorbed CO_2 ($*CO_2$) can undergo dissociation into *CO and O*. However, the energetics differ significantly: CO_2 splitting on Fe(100) is strongly exothermic, consistent with previous DFT studies,[56] while on FeO(100) it is highly endothermic. These contrasting behaviors indicate that CO_2 dissociation is more favorable on Fe(100) than on FeO(100).

The adsorption energy profiles and associated configurations are provided in Tables S6, S7 and Fig. S15–S20, while computational details are described in SI Note 4–6. The full CO_2 splitting half-cycle includes *CO desorption. The strong exothermicity of $*CO_2$ dissociation on Fe(100) results in a strongly bound *CO, requiring 2.15 eV to desorb (Fig. 5a). An alternative pathway involves *CO spillover from Fe(100) to FeO(100), which is uphill by 1.59 eV—still significantly lower than the direct desorption energy from Fe(100) (Fig. 5a and c). From the FeO(100) surface, *CO desorption requires only 0.56 eV, making this spillover route a plausible and kinetically accessible CO release pathway (Fig. 5b). We assign this as the "fast" process. In contrast, the "slow" process corresponds to direct *CO desorption from Fe(100), which is hindered by its strong binding. Nevertheless, this desorption becomes progressively easier as the surface *CO coverage increases (SI Note 7 and Fig. S21, S22), consistent with previous theoretical findings.[57] Finally, the remaining O* can either remain on Fe(100) or migrate to FeO(100). As the surface O* coverage increases, oxidation of Fe and FeO occurs, leading to the formation of Fe_3O_4 through phase transformation (detailed in SI Note 8 and Fig. S23). Experimentally, when the H_2 pulse duration is increased, the FeO content decreases. This suggests

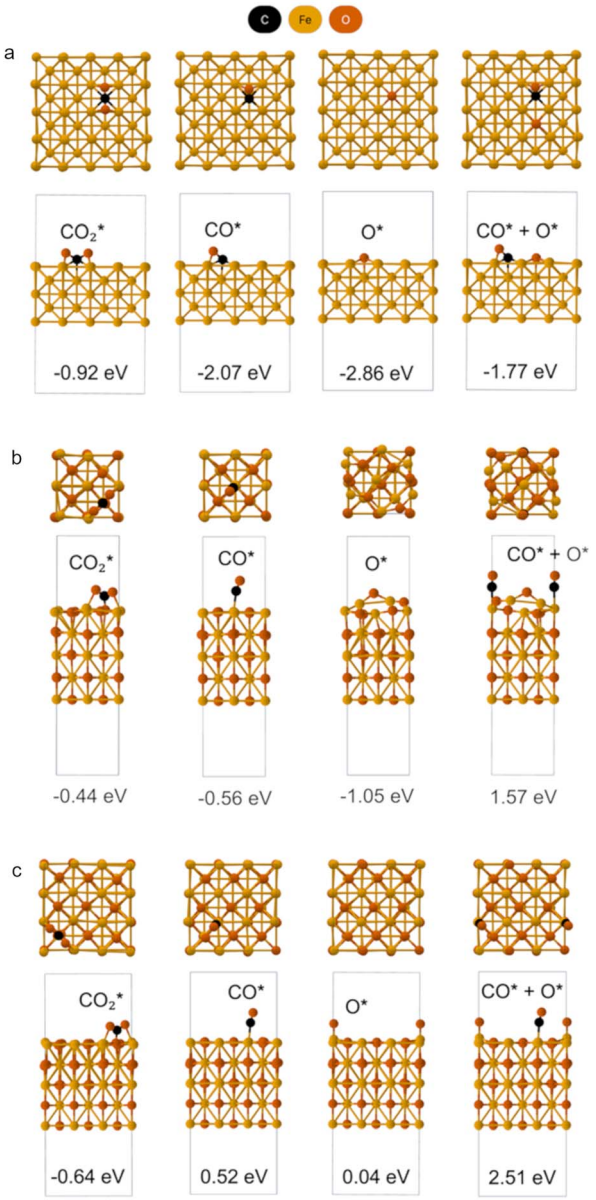

Fig. 4 Top and side views of the most stable CO_2^*, CO*, O*, and CO* + O* adsorption configurations on (a) 4 × 4 × 5 Fe(100), (b) 2 × 2 × 5 FeO(100), and (c) 3 × 3 × 5 FeO(100) surfaces. The numerical values denote the adsorption energies (E_{ads}) for CO_2^* CO*, and O* species, and the dissociative adsorption energy (ΔE_{chem}) for the CO* + O* states.

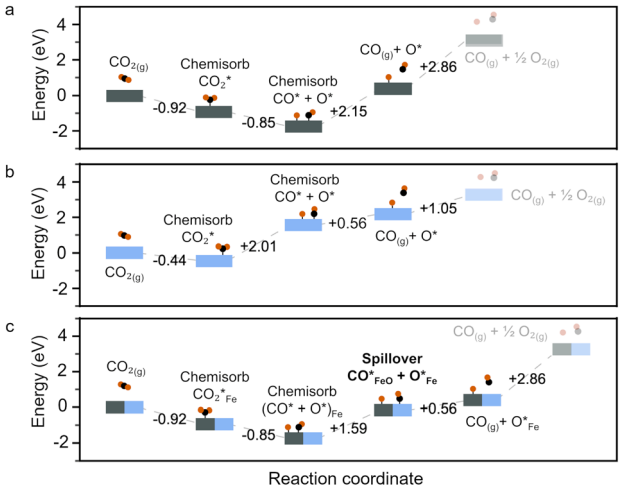

Fig. 5 Relative energy diagrams for CO_2 splitting on Fe(100), FeO(100), and the Fe(100)/FeO(100) interface. (a) CO_2RR pathway on the FeO(100) surface. (b) CO_2-splitting pathway on the Fe(100) surface. (c) Reaction pathway on the Fe(100)/FeO(100) interface from gaseous CO_2 to the final desorbed CO(g) and $\frac{1}{2}O_2$(g). Subscripts (Fe or FeO) indicate the surface hosting each intermediate. The key transition—*CO spillover from Fe(100) to FeO(100)—is highlighted in bold. Adsorption energies correspond to the most stable configurations identified in Tables S5 and S6.

that the contribution of the fast CO release pathway is reduced, forcing the system to rely on the slower desorption route, where *CO must accumulate on Fe before desorption becomes thermodynamically favorable. The observed suppression of CO release is attributed to the strong *CO binding on Fe(100), which not only impedes desorption but also passivates the surface, inhibiting further CO_2 splitting and thus preventing Fe oxidation to Fe_3O_4, explaining the experimental results.

Note that our DFT calculations employ ideal, defect-free Fe(100) and FeO(100) slab models, neglect vibrational free-energy contributions, and do not explicitly locate transition states that determine kinetic barriers. We also did not consider surface defects or strain,[58,59] both of which could modulate CO_2 dissociation barriers and CO adsorption and thereby affect CO spillover at the Fe/FeO interface. A more rigorous description would therefore require incorporating these effects explicitly. Despite these simplifications, the computed adsorption energetics reproduce the qualitative experimental behavior, suggesting that the dominant features governing the chemical-looping process are captured. A systematic assessment of defect and strain effects, and the potential for performance optimization *via* defect engineering, will be an important direction for future work.

Further discussion on the structural properties of the reduced oxygen carrier and their relations to CO_2-splitting performance

The roles of the mole fraction and grain size of Fe and FeO are further discussed by plotting the *n*-values and *k*-values with respect to these structural properties. In general, the *n*-value decreases as the grain size of Fe (d_{Fe}) and FeO (d_{FeO}) increases (Fig. 6a and b). It also showed a positive correlation with the abundance of FeO (X_{FeO}) but a negative correlation with the Fe content (X_{Fe}) (Fig. 6c and d). The small grains of Fe (d_{Fe}) and FeO (d_{FeO}) and the abundance of FeO (X_{FeO}) with adequate amounts of Fe (X_{FE}) in the 3 min/3 min program made it stand out among others, giving rise to its 2D oxide growth during the CO_2-splitting step. Similar results were observed for the *k*-value; it decreases as d_{Fe} and d_{FeO} increase (Fig. 6e and f). It showed a positive correlation with X_{FeO} but a negative correlation with X_{Fe} (Fig. 6g and h). Our results suggested that large amounts of small size FeO and Fe grains in the oxygen carrier created

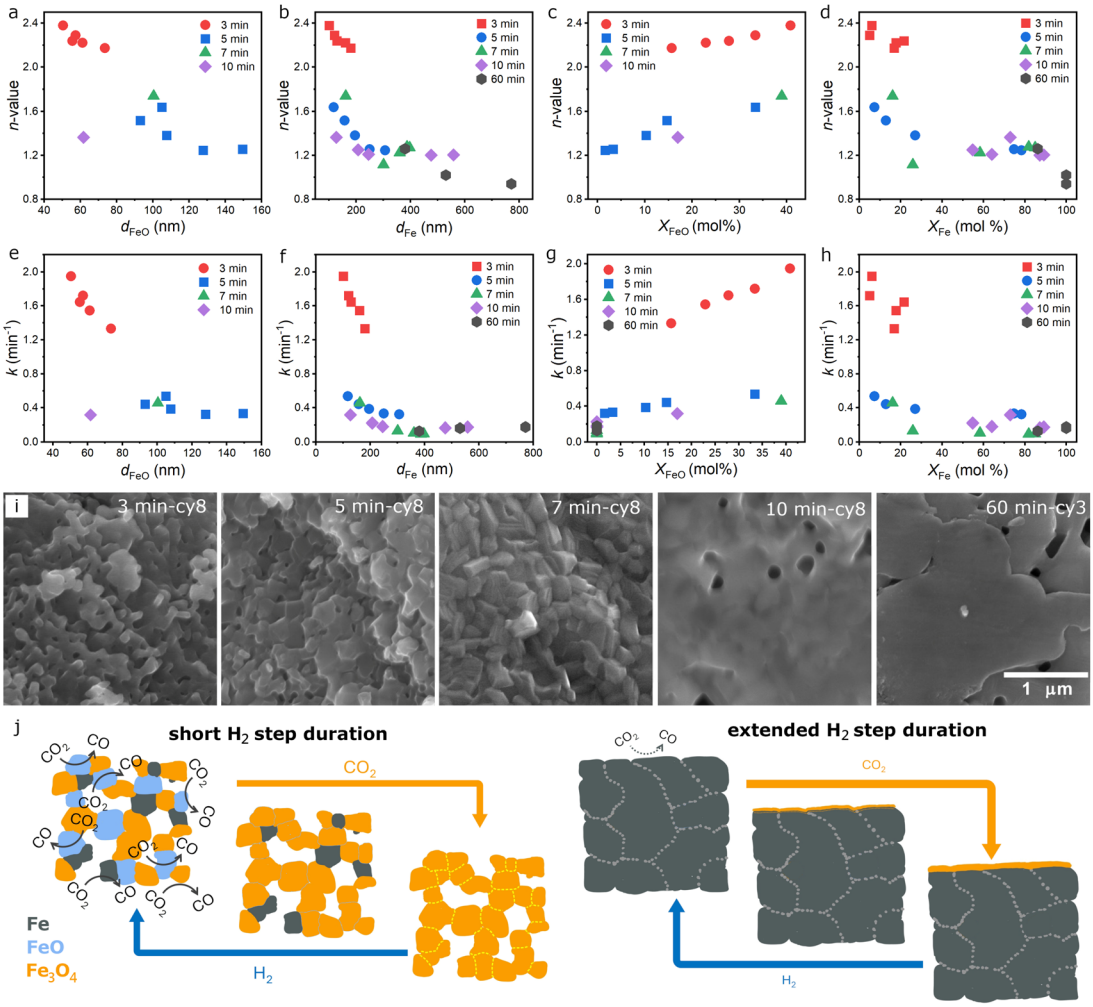

Fig. 6 Discussion on the descriptor for fast CO_2-splitting kinetics. Correlation of (a–d) *n*-value and (e–h) *k*-value with respect to the grain size and mole fraction of FeO and Fe, respectively. (i) Morphological features of the oxygen carriers examined by SEM after subjected to different CL programs. (j) Schematic illustration of the proposed structure–property relationship of the Fe-oxygen carrier for CL CO_2-splitting.

optimum CO_2 dissociation pathways and were responsible for the additional growth dimension and fast kinetics in the short-H_2 CL programs.[60] Microstructure characterization from scanning electron microscopy (SEM) provided additional insights into the varying behaviors of the oxygen carrier in different programs (Fig. 6i and S24). A significant transition in morphology can be observed as the H_2-step duration increased. From the micrograph of the oxygen carrier taken after the 8th H_2-step in the 3 min/10 min program, it reveals that the material was not only formed of small-size grains but also exhibited a porous structure. High resolution scanning transmission electron microscopy (STEM) imaging from the same but crushed sample suggested that particles observed in the SEM were composed of a uniform mixture of small grain-size Fe, FeO, and Fe_3O_4, since the coupled EDS spot analysis of 13 particles was very similar (Fig. S25).Furthermore, a fine nanoporous structure was identified from the dark-field STEM image (Fig. S26). The nanoporosity and small particle size, with narrow size and composition distributions, provide a suitable condition for 2-D oxide growth with fast kinetics.[16] When increasing the H_2-step duration to 5 min, the oxygen carrier evolved into layered materials formed of larger plate-like particles with much decreased void space. STEM-EDS analysis also revealed the formation of large particles that were dominated by metallic Fe (Fig. S27). This resulted in a significant drop in the *n*-value and *k*-value as a significant fraction of the oxygen carriers became large metallic Fe particles, which was only capable of 1-D oxide growth with much slower kinetics. The 7 min/10 min program had evolved the oxygen carrier into densely packed particles of high crystallinity. The absence of void space resulted in 1-D oxide growth with slow kinetics. However, sintering into larger grains seemed to be impeded under this operating condition. Further increase in the H_2 step duration to 10 min resulted in the formation of a continuous Fe over-layer covering the more faceted particles. Finally, only sintered large particles can be observed at a long H_2-step of 60 min. Based on the detailed characterization of the oxygen carrier, we proposed that the high CO_2-splitting kinetics and cycle stability was enabled by the high content of small size FeO and the nanoporous structure of the oxygen carrier created in the CL process

with short H_2 steps (Fig. 6j). Sintered large Fe particles formed in extended H_2 steps can react with CO_2 only through their surface layer with limited reactivity while the bulk becomes inaccessible to further oxidation. Although we have identified the critical role of FeO in low temperature CO_2 splitting and operational conditions to maximize its regeneration, the issue of performance loss over time is not yet resolved. This is due to the irreversible growth of particle size and loss of nanoporous structure.

Conclusions

The ability of pure iron oxygen carriers to conduct CO_2-splitting in a chemical looping process is revisited using RWGS as a model reaction. Through thorough kinetic, thermochemical, and structural analysis, the relationship between the crystal/morphological structure of the oxygen carrier with its CO_2-splitting performance was mapped out. With controlled reduction, the nanoporous oxygen carrier with high FeO content showed exceptional reactivity towards CO_2-splitting at temperatures as low as 350 °C. Kinetic and structural analyses suggest that the nanoporous structure contributes to a 2-D oxide growth, while the high FeO content promotes the intrinsic growth rate. Extended reduction led to the formation of bulky pure metallic iron, which appears to be significantly kinetically impeded towards CO_2-splitting under identical conditions. DFT calculation suggested the minimum energy pathway for CO_2 dissociation and subsequent CO desorption under the coexistence of metallic Fe and wustite FeO. The findings in this work may provide alternative thinking in the design of the oxygen carriers and CL-CCU operations from a materials aspect focusing on kinetically controlled structural reversibility.

Author contributions

The manuscript was written through contributions of all authors. All authors have given approval to the final version of the manuscript.

Conflicts of interest

There are no conflicts to declare.

Data availability

The data supporting this article have been included as part of the supplementary information (SI). Supplementary information is available. See DOI: https://doi.org/10.1039/d5ta07934a.

Acknowledgements

This research was financially supported by the Industrial Technology Research Institute (ITRI) with grant no. N354DA7210. This research was also supported by the National Science and Technology Council (NSTC) of Taiwan with grant no. 112-2221-E-007-020-MY3 and 112-2628-E-007-011-MY3 on the advanced characterization *via* EM of the Instrumentation Center at National Tsing Hua University (NTHU). This research was also supported by the National Science and Technology Council (NSTC) of Taiwan with grant no. 114-2628-E-007-002 on computational studies. We thank the National Center for High-performance Computing (NCHC) for providing computational and storage resources.

References

1 G. G. Esquivel-Patiño, F. Nápoles-Rivera and A. Jiménez-Gutiérrez, *Energy Convers. Manag.*, 2023, **295**, 117619.
2 Å. Eliasson, E. Fahrman, M. Biermann, F. Normann and S. Harvey, *Int. J. Greenhouse Gas Control*, 2022, **118**, 103689.
3 D. Bhalothia, W.-H. Hsiung, S.-S. Yang, C. Yan, P.-C. Chen, T.-H. Lin, S.-C. Wu, P.-C. Chen, K.-W. Wang, M.-W. Lin and T.-Y. Chen, *ACS Appl. Energy Mater.*, 2021, **4**, 14043–14058.
4 C. Yan, C.-H. Wang, M. Lin, D. Bhalothia, S.-S. Yang, G.-J. Fan, J.-L. Wang, T.-S. Chan, Y.-l. Wang, X. Tu, S. Dai, K.-W. Wang, J.-H. He and T.-Y. Chen, *J. Mater. Chem. A*, 2020, **8**, 12744–12756.
5 T. A. Le, M. S. Kim, S. H. Lee, T. W. Kim and E. D. Park, *Catal. Today*, 2017, **293–294**, 89–96.
6 L. Shen, J. Xu, M. Zhu and Y.-F. Han, *ACS Catal.*, 2020, **10**, 14581–14591.
7 D.-H. Tsai, T.-T. Wu, H.-C. Lin, L.-Y. Chueh, K.-H. Lin, W.-Y. Yu and Y.-T. Pan, *Chem.–Asian J.*, 2024, **19**, e202300955.
8 H.-X. Liu, S.-Q. Li, W.-W. Wang, W.-Z. Yu, W.-J. Zhang, C. Ma and C.-J. Jia, *Nat. Commun.*, 2022, **13**, 867.
9 Y.-F. Shi, P.-L. Kang, C. Shang and Z.-P. Liu, *J. Am. Chem. Soc.*, 2022, **144**, 13401–13414.
10 M. Bowker, *ChemCatChem*, 2019, **11**, 4238–4246.
11 S. Abanades and A. Le Gal, *Fuel*, 2012, **102**, 180–186.
12 Y. Feng, N. Wang, X. Guo and S. Zhang, *Fuel*, 2020, **262**, 116489.
13 V. V. Galvita, H. Poelman, V. Bliznuk, C. Detavernier and G. B. Marin, *Ind. Eng. Chem. Res.*, 2013, **52**, 8416–8426.
14 N. S. Yüzbasi, A. Armutlulu, T. Huthwelker, P. M. Abdala and C. R. Müller, *J. Mater. Chem. A*, 2022, **10**, 10692–10700.
15 L. Zeng, Z. Cheng, J. A. Fan, L.-S. Fan and J. Gong, *Nat. Rev. Chem.*, 2018, **2**, 349–364.
16 A. A. Sunny, Q. Meng, S. Kumar, R. Joshi and L.-S. Fan, *Acc. Chem. Res.*, 2023, **56**, 3404–3416.
17 X. Zhu, Q. Imtiaz, F. Donat, C. R. Müller and F. Li, *Energy Environ. Sci.*, 2020, **13**, 772–804.
18 W.-Z. Hung, Z. X. Law, D.-H. Tsai, B.-H. Chen, C.-H. Chen, H.-Y. Hsu and Y.-T. Pan, *MRS Energy Sustain*, 2022, **9**, 342–349.
19 Y. Fan, B. Jin, Q. Guo and Z. Liang, *ACS Sustain. Chem. Eng.*, 2023, **11**, 5999–6010.
20 J. Rojas, E. Sun, G. Wan, J. Oh, R. Randall, V. Haribal, I.-h. Jung, R. Gupta and A. Majumdar, *ACS Sustain. Chem. Eng.*, 2022, **10**, 12252–12261.
21 V. V. Galvita, H. Poelman, C. Detavernier and G. B. Marin, *Appl. Catal. B*, 2015, **164**, 184–191.
22 T. Ouyang, B. Jin, Y. Mao, D. Wei and Z. Liang, *Appl. Catal. B*, 2024, **343**, 123531.
23 J. Zhang, V. Haribal and F. Li, *Sci. Adv.*, 2017, **3**, e1701184.

24 Y. Qiu, L. Ma, M. Li, D. Cui, S. Zhang, D. Zeng and R. Xiao, *Chem. Eng. J.*, 2020, **387**, 124150.
25 L. Liu and M. R. Zachariah, *Energy Fuels*, 2013, **27**, 4977–4983.
26 L.-l. Wang, L.-h. Shen, W. Liu and S. Jiang, *Energy Fuels*, 2017, **31**, 8423–8433.
27 F. He, Z. Huang, G. Wei, K. Zhao, G. Wang, X. Kong, Y. Feng, H. Tan, S. Hou, Y. Lv, G. Jiang and Y. Guo, *Energy Convers. Manag.*, 2019, **201**, 112157.
28 L. Ma, Y. Qiu, M. Li, D. Cui, S. Zhang, D. Zeng and R. Xiao, *Ind. Eng. Chem. Res.*, 2020, **59**, 6924–6930.
29 X. Tian, C. Zheng and H. Zhao, *Appl. Catal. B*, 2022, **303**, 120894.
30 D. Sastre, D. P. Serrano, P. Pizarro and J. M. Coronado, *J. CO_2 Util.*, 2019, **31**, 16–26.
31 F. Li, Z. Sun, S. Luo and L.-S. Fan, *Energy Environ. Sci.*, 2011, **4**, 876–880.
32 Y.-Y. Chen, M. Guo, M. Kim, Y. Liu, L. Qin, T.-L. Hsieh and L.-S. Fan, *Chem. Eng. J.*, 2021, **406**, 126729.
33 Y. e. Zheng, X. Liao, H. Xiao, V. Haribal, X. Shi, Z. Huang, L. Zhu, K. Li, F. Li, H. Wang and X. Chen, *Nano Energy*, 2020, **78**, 105320.
34 G. Kresse and J. Hafner, *Phys. Rev. B: Condens. Matter Mater. Phys.*, 1993, **47**, 558–561.
35 G. Kresse and J. Hafner, *Phys. Rev. B: Condens. Matter Mater. Phys.*, 1994, **49**, 14251–14269.
36 G. Kresse and J. Furthmüller, *Comput. Mater. Sci.*, 1996, **6**, 15–50.
37 G. Kresse and J. Furthmüller, *Phys. Rev. B: Condens. Matter Mater. Phys.*, 1996, **54**, 11169–11186.
38 V. Wang, N. Xu, J.-C. Liu, G. Tang and W.-T. Geng, *Comput. Phys. Commun.*, 2021, **267**, 108033.
39 J. P. Perdew and W. Yue, *Phys. Rev. B: Condens. Matter Mater. Phys.*, 1986, **33**, 8800–8802.
40 J. P. Perdew, J. A. Chevary, S. H. Vosko, K. A. Jackson, M. R. Pederson, D. J. Singh and C. Fiolhais, *Phys. Rev. B: Condens. Matter Mater. Phys.*, 1992, **46**, 6671–6687.
41 P. E. Blöchl, *Phys. Rev. B: Condens. Matter Mater. Phys.*, 1994, **50**, 17953–17979.
42 G. Kresse and D. Joubert, *Phys. Rev. B: Condens. Matter Mater. Phys.*, 1999, **59**, 1758–1775.
43 M. Methfessel and A. T. Paxton, *Phys. Rev. B: Condens. Matter Mater. Phys.*, 1989, **40**, 3616–3621.
44 R. F. W. Bader, *Acc. Chem. Res.*, 1985, **18**, 9–15.
45 G. Henkelman, A. Arnaldsson and H. Jónsson, *Comput. Mater. Sci.*, 2006, **36**, 354–360.
46 E. Sanville, S. D. Kenny, R. Smith and G. Henkelman, *J. Comput. Chem.*, 2007, **28**, 899–908.
47 W. Tang, E. Sanville and G. Henkelman, *J. Phys. Condens. Matter.*, 2009, **21**, 084204.
48 M. Yu and D. R. Trinkle, *J. Chem. Phys.*, 2011, **134**, 064111.
49 A. Jain, S. P. Ong, G. Hautier, W. Chen, W. D. Richards, S. Dacek, S. Cholia, D. Gunter, D. Skinner, G. Ceder and K. A. Persson, *APL Mater.*, 2013, **1**, 011002.
50 M. Avrami, *J. Chem. Phys.*, 1939, **7**, 1103–1112.
51 J. D. Hancock and J. H. Sharp, *J. Am. Ceram. Soc.*, 1972, **55**, 74–77.
52 K. Piotrowski, K. Mondal, T. Wiltowski, P. Dydo and G. Rizeg, *Chem. Eng. J.*, 2007, **131**, 73–82.
53 Q. Tang and K. Huang, *Chem. Eng. J.*, 2022, **434**, 134771.
54 W. K. Jozwiak, E. Kaczmarek, T. P. Maniecki, W. Ignaczak and W. Maniukiewicz, *Appl. Catal. A*, 2007, **326**, 17–27.
55 M. H. Jeong, D. H. Lee, G. Y. Han, C.-H. Shin, M. K. Shin, C. K. Ko and J. W. Bae, *Fuel*, 2017, **202**, 547–555.
56 X. Liu, L. Sun and W.-Q. Deng, *J. Phys. Chem. C*, 2018, **122**, 8306–8314.
57 T. Wang, X. Tian, Y.-W. Li, J. Wang, M. Beller and H. Jiao, *J. Phys. Chem. C*, 2014, **118**, 1095–1101.
58 A. Chakrabarty, E. T. Bentria, S. A. Omotayo, O. Bouhali, N. Mousseau, C. S. Becquart and F. El Mellouhi, *Appl. Surf. Sci.*, 2019, **491**, 792–798.
59 D. C. Sorescu, D. L. Thompson, M. M. Hurley and C. F. Chabalowski, *Phys. Rev. B: Condens. Matter Mater. Phys.*, 2002, **66**, 035416.
60 Q. Jiang, Y. Gao, V. P. Haribal, H. Qi, X. Liu, H. Hong, H. Jin and F. Li, *J. Mater. Chem. A*, 2020, **8**, 13173–13182.

